

Mössbauer spectroscopy of conversion electrons: determining the range of depths that can be analyzed by nondestructive depth profiling

A. I. Chumakov and G. V. Smirnov

I. V. Kurchatov Institute of Atomic Energy

(Submitted 30 May 1985)

Zh. Eksp. Teor. Fiz. 89, 1810–1823 (November 1985)

The range of depths that can be probed through detection of electrons of various energies is determined for 14.4 keV gamma-rays interacting with an iron target. The range of depths is found by measuring the angular dependence $\kappa(\theta)$ of the photoelectron emission near the critical angle θ_{cr} for total external reflection of the gamma-rays by the target. The conditions in Mössbauer experiments are simulated by selecting x rays of appropriate energy from the white x-ray bremsstrahlung. A superposition technique for achieving improved layer localization is described which is both quick and versatile (applicable to specimens of arbitrary structure). In addition, only one specimen is required, and all the data can be obtained in a single experiment.

1. INTRODUCTION

Recording the inelastic decay products of excited nuclei is currently an important and rapidly developing method for analyzing the resonant interaction of nuclear γ -radiation with matter. Particularly informative results can be obtained by detecting the internal conversion electrons (conversion-electron Mössbauer spectroscopy). The unique features of this method include the capability of probing the chemical composition and structure of surfaces¹ (particularly for such interesting materials as amorphous metals and alloys²), and the fact that it permits one to analyze the structure of the wave fields that are generated in crystals when Mössbauer radiation interacts coherently with matter.³

Depth profiling (layer-by-layer analysis of sample properties) based on recording the Mössbauer spectra of conversion electrons selectively at various depths x represents a new stage in the development of conversion-electron Mössbauer spectroscopy. This selective “depth profiling” technique is nondestructive and can be carried out simultaneously for several layers. Since the technique exploits the relation between the final electron energy E_f and the path-length λ of the electrons in the material, one can vary the depths probed by selecting electrons that reach the surface with a given E_f . Selective depth profiling can make the experiments much more informative and can also be used to study the chemical composition of different layers,¹ variations in the hyperfine magnetic field with depth,⁴ etc.

In depth-profiling experiments it is essential to determine the range of depths from which electrons of given energy are emitted, and until recently these depths could only be estimated. Theoretical calculations that simulate electron emission from solid targets are of limited use, because it is difficult to accommodate the specific properties of the electron detectors (their energy resolution, efficiency, collection angle, etc.).

Several experimental methods are currently available for determining the depth ranges for electrons of arbitrary final energy^{5–7}; however, they apply only to materials with a perfect single-crystal structure and are unlikely to find much use in conversion-electron Mössbauer spectroscopy, where perfect specimens are extremely uncommon.

The method proposed in Ref. 8 for finding the range of depths that can be probed using electrons of given energy applies to specimens of arbitrary structure. However, it is far from simple because it requires preparing numerous samples, which must be coated by films of precisely measured thickness whose isotope composition differs from that of the substrate. It will thus be of interest to develop a simpler and more generally applicable technique in which all the necessary experimental data can be obtained from a single specimen of arbitrary structure. We suggest a method which is based on measuring the angular dependence of the photoelectron emission near the critical angle θ_{cr} for total external reflection,^{9,10} and in the present work we employ it to directly measure the range of depths that can be probed by selective detection of conversion electrons for the case when 14.4 keV γ -rays interact with an iron target. Because of their wide practical applications and the fact that the ⁵⁷Co:⁵⁷Fe “source-absorber” pair is the one most commonly used in Mössbauer spectroscopy, it will be of particular interest to determine the range of depths for ⁵⁷Co and ⁵⁷Fe.

2. PRINCIPLE OF THE METHOD

The yield function concept can be used to quantitatively determine the depth interval that can be probed by electrons of a given energy.¹¹ The yield function for electrons of final energy E_f in a selected interval is defined as the probability density $P(x)$ for such electrons to emerge at the surface from a depth x inside the target.

The waves scattered by individual atoms are well-known to add coherently in small-angle scattering experiments to give a wave which is diffracted at a small angle and is coherent with the incident wave. Because of the interference between the incident and reflected waves, the wave field is forced out toward the surface as the angle of incidence θ of the radiation decreases. The angular dependences $R(\theta)$ and $T(\theta)$ of the reflected and transmitted waves are given by (see, e.g., Ref. 12)

$$R(\theta) = \left| \frac{\sin \theta - (\chi + \sin^2 \theta)^{1/2}}{\sin \theta + (\chi + \sin^2 \theta)^{1/2}} \right|^2 ,$$

$$T(\theta, x) = \frac{4 \sin^2 \theta \exp(-q(\theta)x)}{|\sin \theta + (\chi + \sin^2 \theta)^{1/2}|^2},$$

$$q(\theta) = \frac{4\pi}{\lambda} \operatorname{Im}(\chi + \sin^2 \theta)^{1/2},$$
(1)

where $T(\theta, x)$ is the intensity of the wave field at depth x in the target, $\chi = \chi_r + i\chi_i$ is the complex effective polarizability of the medium, $q(\theta)$ is the attenuation coefficient, and λ is the wavelength of the radiation.

As θ decreases and the field is forced out to the surface, the photoelectric effects terminates, first in the interior and then closer and closer to the surface. The normalized photoemission $\kappa(\theta)$ for each group of electrons is obtained by dividing the photoemission by the yield at normal incidence (i.e., the photoemissions of all the electron groups are taken to have unit amplitude at normal incidence). Then as θ decreases, $\kappa(\theta)$ for electrons originating at greater yield depths x will be less than $\kappa(\theta)$ for electrons emerging from close to the surface. The angular dependences $\kappa(\theta)$ thus contain information about the yield depth, i.e., on $P(x)$ for electrons with final energies in a given range. This fact is exploited in our method.

The angular dependences $\kappa(\theta)$ for electrons with a yield function $P(x)$ are given by the expression⁹

$$\kappa(\theta) = \frac{N_e(\theta)}{N_e(\pi/2)} = \frac{1}{\sin \theta} \int_0^\infty T(\theta, x) P(x) dx.$$
(2)

Here $N_e(\pi/2)$ is the corresponding electron yield at normal incidence. The field intensity in the target is normalized by the intensity of the incident wave, and P is normalized by

$$\int_0^\infty P(x) dx = 1.$$
(3)

We assume that the penetration depth $L(\pi/2)$ of the field at normal incidence is much greater than the depths x at which the electrons originate. The unknown function $P(x)$ can be found by using standard methods to solve the integral equation (2).

In order to find $P(x)$ one must thus measure the angular dependence $\kappa(\theta)$ of the photoemission and correctly choose the kernel $T(\theta, x)$ in (2), i.e., the angular depen-

dence of the intensity of the wave field inside the target (this requires correcting for the divergence of the incident radiation beam, etc.).

3. EXPERIMENT

The target was an iron strip of dimensions $30 \times 8 \times 2$ mm which was polished to grade-14 smoothness (surface irregularities of height less than 300–500 Å), and the measurements were carried out in a two-crystal diffraction configuration (Fig. 1). We simulated the conditions in Mössbauer experiments by selecting the 14.4 keV component from the x-ray bremsstrahlung. The radiation was collimated and made monochromatic by reflection from a silicon crystal (symmetric [111] reflection) and passing it through the narrow ($30 \mu\text{m}$) entrance slit of a monochromator. Since the diffraction angles on the iron strip and at the monochromator crystal differed greatly, the angular divergence of the beam was due primarily to dispersion. The divergence of the beam reflected by the silicon crystal was measured to be $60''$ and $20''$ in the horizontal and vertical planes.

We measured $P(x)$ for the iron strip by placing it inside a gas-flow proportional counter. The electron detector was specially designed to measure the photoemission at θ_{cr} , the critical angle for total external reflection of the x-rays (we benefited here from the experience gained in operating an earlier detector model described in Ref. 13). The geometry of the counter ensured that the electrons were collected under identical conditions from all parts of the irradiated region, and that the electron recording efficiency was independent of the length of the irradiated region. The energy resolution of the counter was $\approx 18\%$.

The counter was mounted on a goniometer and rotated at a constant velocity of $0.03''/\text{sec}$. The measurement cycle involved measuring the total energy spectrum of the emitted electrons and recording it on magnetic tape; the cycle was repeated every 1000 m. We recorded 50 spectra, each corresponding to an angular interval of $0.5'$. A "NOKIA" LP-4900 multichannel automatic pulse analyzer was used, and the maximum electron counting rate was 250 pulses/s for an incident flux of ~ 350 photons/s on the iron target. We used a scintillation detector to record the reflected beam while

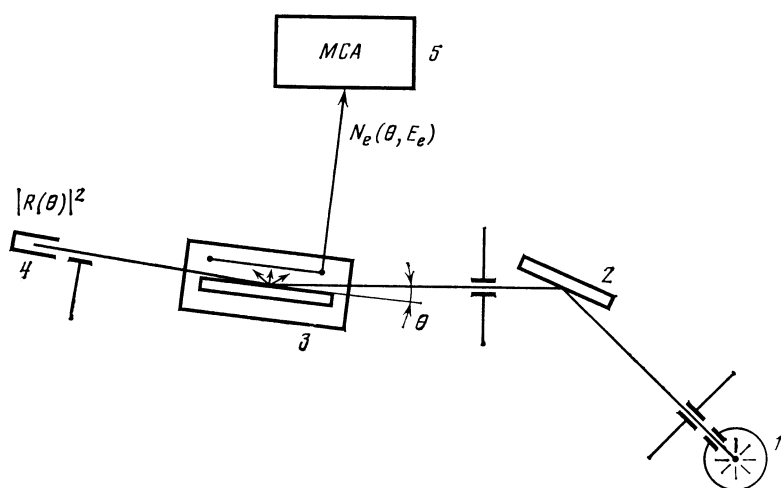


FIG. 1. Schematic of experimental configuration: 1) x-ray source ($E = 14.4$ keV); 2) silicon monochromator ($\{111\}$ reflection); 3) iron target inside a gas-filled proportional electron counter; 4) scintillator for detecting the reflected beam; 5) automatic multichannel pulse analyzer.

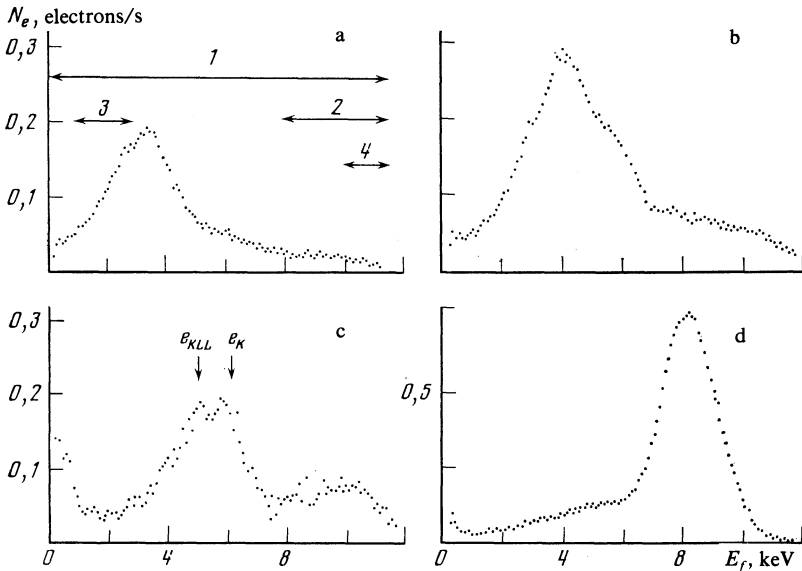


FIG. 2. Measured energy spectra $N_e(E_f)$ of the photoemission for incident angle $\theta = 36, 22$, and $12'$ (a–c, respectively). The K -shell photoelectrons (e_K), Auger electrons (e_{KLL}), and several other groups (1–4) with selected energy ranges are shown. d) The electron energy spectrum used for calibration (the electrons were generated in the counter by $Cu K_\alpha$ radiation).

measuring the photoemission. All the measurements were made in a single angular sweep of the target, and the experiment took 10 hours.

The primary experimental results were the angular dependence $R(\theta)$ of the reflection coefficient and a two-dimensional body of data giving the photoemission intensity as a function of θ and the final energy E_f of the electrons arriving at the surface of the iron strip.

4. MEASUREMENT RESULTS

The successive changes in the photoemission spectrum were due to the expulsion of the wave field toward the surface of the target as the angle of incidence decreased. The incident energy was $E_\gamma = 14.4$ keV, and the energies of the K - and L -shells for atomic iron are equal to $E_K = 7.1$ keV and $E_L = 0.7$ keV. Under these conditions, the production of 100 photoelectrons of initial energy $E_1 = 7.3$ keV was accompanied by the generation of 70 Auger electrons of initial energy $E_2 = 5.7$ keV. The stopping lengths (more precisely, the Bethe lengths, see, e.g., Ref. 11) for these electrons are equal to $R_{B1} = 3700 \text{ \AA}$ and $R_{B2} = 2300 \text{ \AA}$, respectively. Figure 2a–c shows some measured photoemission energy spectra for incident angles $\theta = 36, 22$, and $12'$. The energy scale was calibrated by passing a beam of $Cu K_\alpha$ radiation directly through the counter without any target; we found the value 8 keV for the energy of the photoelectrons generated in the gas indicated. The energy resolution of the detector can be characterized in terms of the width of the recorded energy spectrum (Fig. 2d).

The energy calibration showed that for $\theta = 36'$, the electrons reaching the surface had large energy losses. This is hardly surprising, since they had to cross a layer of width $\approx 1500 \text{ \AA}^1$ before reaching the surface, which is comparable to the maximum depths for the Auger and photoelectrons.

The energy spectrum contains a broad peak which is composed of the signals from strongly retarded Auger photoelectrons. In addition, the high-energy part of the spec-

trum consists of the signals generated when two electrons reached the target surface simultaneously. These signals coalesce, and the amplitude is proportional to the sum of the energies of the two electrons. This type of coincidence is most likely for Auger and photoelectrons which are generated in a single atom.

When θ is decreased to $22'$ the energy spectrum shifts appreciably toward higher energies, because in this case the field penetration depth in the target is just $L = 800 \text{ \AA}$, so that the electrons lose less energy. Two groups of electrons with different energies can barely be made out in the peak of the spectrum. Finally, for $\theta = 12'$ two peaks are clearly discernible. In this case, L is only $20\text{--}30 \text{ \AA}$ and the electrons lose hardly any energy at all. The shape of the spectrum depends primarily on the energy resolution of the electron detector. The fact that the peak for the group of coincidences is better-defined also indicates that the electrons are nearly monoenergetic for $\theta = 12'$.

Figure 2a shows the groups of electrons for which $P(x)$ was determined. Range 1 comprises all of the electrons; the corresponding dependences $\chi(\theta)$ and $P(x)$ characterize the average properties of the photoemission and can be measured in experiments which lack energy resolution. Range 2 contains the signals due to coincidences of an Auger electron and a photoelectron generated at the same atom. We note first of all that the average depth for such coincidences is small because the probability is given by the product of the yield probabilities for each electron. In addition, region 2 selects the most energetic of these signals; the corresponding electrons have lost only a small fraction of their initial energy and must therefore originate at small depths x . By contrast, the electrons for range 3 have lost nearly all of their initial energy and should therefore originate at large x . The reasons for considering range 4 will be discussed below.

In order to find how the yield of electrons in a given range of final energies ΔE_f depends on θ , one must integrate the two-dimensional photoemission intensities over ΔE_f . The results are shown in Fig. 3, which plots $\chi(\theta)$, the photoemission normalized by the electron yield at normal inci-

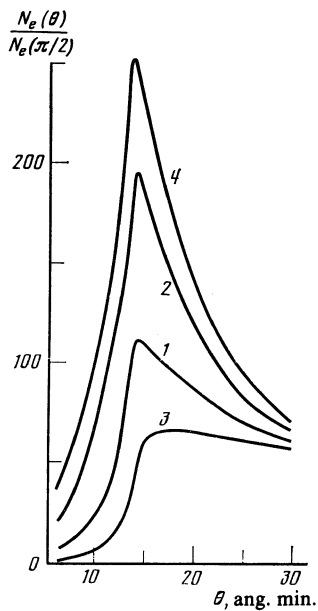


FIG. 3. Normalized photoemission versus incident angle. The curves correspond to the energy ranges 1–4 in Fig. 2a.

dence. The curves $\varkappa(\theta)$ were determined up to a factor C which was equal to unity to within 20–30% and constant for each curve; this uncertainty in the scaling of the vertical axis had no effect on the calculation of $P(x)$. We corrected the curves $\varkappa(\theta)$ for background noise due to absorption of the radiation beam by the gas in the counter.

Figure 4 plots the calculated and measured reflection coefficients $R(\theta)$ and the calculated angular dependence $L(\theta)$ of the field penetration depth in the target. Curve 1 shows that the critical angle was equal to 14 angular minutes. For $\theta \approx 14'$ the intensity of the reflected wave increases

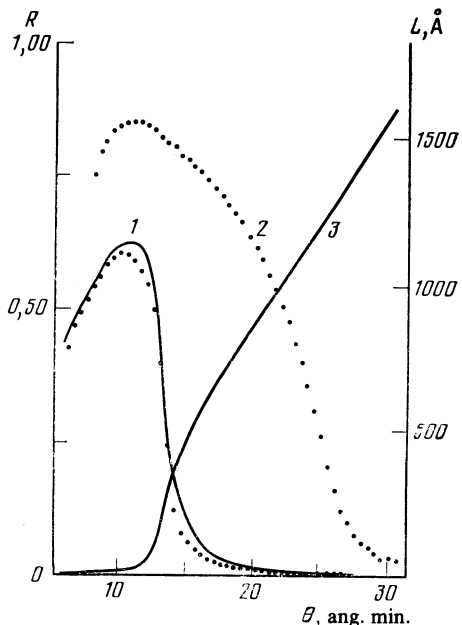


FIG. 4. Experimental points and calculated curves for the reflection coefficient $R(\theta)$ (1, 2), and calculated dependence $L(\theta)$ of the field penetration depth in the target (3). Curves 1 and 3 are for reflection of 14.4 keV x-rays; curve 2 corresponds to reflection of $\text{Cu } K_{\alpha}$ radiation (8.05 keV).

abruptly and should approach a limit ≈ 1 as θ decreases further. However, it actually drops for θ below 10°, apparently because under these conditions not all of the beam strikes the target. In order to verify this explanation and rule out a possible decrease in R due to poor polishing of the target surface, we measured $R(\theta)$ with the 14.4 keV γ -ray source replaced by a $\text{Cu } K_{\alpha}$ 8.05 keV source. Since the critical angle for 8.05 keV radiation is larger (24°), R increased to 0.85 before part of the beam began to miss the target, causing R to drop. This is just 3% less than the theoretical value calculated for $\theta \approx 14'$, which indicates that the target surface was smooth.

The photoemission curves in Fig. 3 differ greatly from one another, even though they were recorded simultaneously during a single angular sweep of the target and differ only in the energy composition of the electrons. The difference is due entirely to the fact that electrons with different final energies originate from different depths in the target. The high sensitivity of the curves $\varkappa(\theta)$ to the yield depth x permits one to find $P(x)$ accurately by solving Eq. (2).

The behavior of $\varkappa(\theta)$ becomes obvious if we transform (2) slightly to

$$\varkappa(\theta) = \frac{1}{\sin \theta} I_0(\theta) \int_0^\infty \exp\{-q(\theta)x\} P(x) dx \propto S(\theta) I_0(\theta) L(\theta), \quad (4)$$

where the dimensionless factors $L(\theta)$ and $S(\theta)$ can be regarded as the depth and the area of the portion of the target from which the electrons are recorded. With this definition, $L(\theta)$ is equal to the field penetration depth in the target or to the electron yield depth x , whichever is smaller. The factor $I_0(\theta)$, the intensity of the wave field at the target surface, is of order unity²⁾ and independent of E_f ; to first approximation it may be neglected. The photoemission then depends only on the volume $L(\theta)S(\theta)$ of the region from which the electrons are recorded. For large θ , the yield depth x is much less than L , so that x determines $L(\theta)$. Under these conditions, the only variable remaining in (4) is the dependence $S(\theta)$ of the area irradiated by the incident radiation beam; S increases as $1/\sin \theta$ with decreasing θ . The photoemission intensity for electrons with $x < L$ therefore also increases as $1/\sin \theta$ (Fig. 3, curve 2). This behavior is particularly prominent for electrons corresponding to range 2 in Fig. 2a.

On the other hand, the yield depth x should be large for the electrons in range 3 (Fig. 2a); in this case $L(\theta)$ quickly becomes less than x , so that L now determines the depth from which the electrons are recorded. Curve 3 in Fig. 4 shows that L is proportional to $\sin \theta$ for a wide range of incident angles, so that the product $S(\theta)L(\theta)$ becomes independent of θ . Thus $\varkappa(\theta)$ has a plateau, which is particularly evident for electrons with E_f in range 3 (Fig. 3, curve 3).

If θ decreases further below the critical angle, L drops abruptly (Fig. 4, curve 3). This is not offset by the increase in $S(\theta)$, and $\varkappa(\theta)$ therefore drops abruptly at all energies. Since the residual photoemission is proportional to the probability that an electron with E_f in a given interval will reach the surface from the uppermost layers, it is greatest for the fast electrons in range 2 (cf. Fig. 3).

5. ANALYSIS OF THE MEASUREMENT RESULTS: CALCULATION OF $P(x)$

Figure 4 compares $R(\theta)$ measured experimentally with the theoretically calculated curve. The latter was found with allowance for the angular divergence of the beam (measured in advance) and for the finite cross section of the radiation beam and the finite target dimensions. We assumed a "rough surface" target model and considered deviations $\Delta\psi$ of the inclination angle of the surface from the average value $\bar{\psi}$ (this deviation gave rise to an additional effective scatter in the incident angle θ of the beam); the model also treated the nonuniform intensity distribution $I(\theta)$ of the incident wave and the shadowing of the reflected rays by rough surface projections. The only undetermined parameter in the model was the magnitude of the spread $\Delta\psi$. Curve 1 in Fig. 4 shows the results of a best-fit analysis of the experimental data; the "goodness" criterion was that the slopes $dR(\theta)/d\theta$ should be the same near the critical angle θ_{cr} . Best agreement was achieved for $\Delta\psi = 5'$, which indicates that the target surface was quite smooth.

We see that the theoretical calculation approximates the experimental results quite closely. The small discrepancy could be due to the presence of the thin oxide film on the surface (the refractive index n of the film differed from n for pure iron—see, e.g., Ref. 14).

In order to solve (2) we calculated values of the kernel $T(\theta, x)$, i.e., the intensity of the wave field inside the target as a function of the angle of incidence and depth. These calculations used Eq. (1) and allowed for surface irregularities; we also used the value $\Delta\psi = 5'$ found by the best-fit analysis. We then attempted to deduce $P(x)$ by solving (2).

Unfortunately, serious problems arose because of inadequacies of the theoretical model [these same inadequacies were responsible for the discrepancy between the measured (curve 1, Fig. 4) and calculated curves $T(\theta, x)$ noted above]. The solution turned out to be unstable to small changes in the photoemission $\chi(\theta)$, and the instability was clearly due to the discrepancy between the calculated dependence $T(\theta, x)$ and the actual behavior of the field, on which $\chi(\theta)$ depends. We therefore had to develop an alternative method for finding $T(\theta, x)$, preferably one based on experimental data (e.g., as in Ref. 6).

Expression (4) depends implicitly on $T(\theta, x)$ through the two factors $I_0(\theta)$ and $L(\theta)$, the wave field intensity at the surface and the field penetration depth in the target, respectively. We found that $I_0(\theta)$ can be deduced from measurements without any use of theory. We did this by taking the two-dimensional body of data on $N_e(\theta, E_f)$ and integrating it over the highest energy range 4 in Fig. 2a, for which the yield depths are smallest. Indeed, $\chi(\theta)$ for region 4 (Fig. 3) lies above the curves for the other energy ranges. We can estimate the average yield depth for these fast electrons in terms of the half-maximum angle $\theta_{1/2}$ for χ . Curve 2 in Fig. 4 shows that the field penetration depth $L(\theta_{1/2})$ is equal to 30 Å; to a good approximation we may therefore take the angular dependence of the yield of electrons in range 4 to be $I_0(\theta)/\sin(\theta)$, the intensity of the wave field at the target surface multiplied by $S(\theta) = 1/\sin \theta$, the area factor

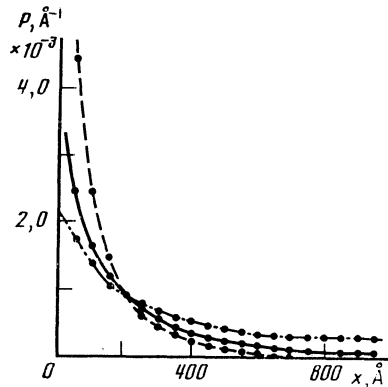


FIG. 5. Relative yield probabilities $P(x)$ calculated from experimental data for final energy ranges 1 (solid), 2 (dashed), and 3 (dash-dotted). The error is 7% for ranges 1, 3 and 17% for range 2.

for the irradiated surface. As before, the factor $1/q(\theta)$ characterizing the field penetration depth into the target was calculated using the rough surface model described above.

With $T(\theta, x)$ found by this procedure, good results were obtained by solving (4) iteratively by an error-minimizing method. Figure 5 shows the yield functions $P(x)$, i.e., the range of depths that can be probed by using electrons with final energies in ranges 1, 2, and 3. The error is estimated at 17% for range 2 and 7% for ranges 1 and 3. The curves $P(x)$ behave as anticipated—the fastest electrons (with the lowest losses) originate much closer to the surface.

6. WAYS TO ENHANCE THE EFFECTIVENESS OF DEPTH PROFILING

The yield probability functions in Fig. 5 have immediate applications to selective depth profiling in resonance Mössbauer experiments with ^{57}Co sources. This is because the rearrangement of the atomic electron shell is independent of how the electron is ejected from the K -shell (whether by photoionization or by conversion).

Unfortunately, it is not possible to localize the layers in the interior of the sample, because $P(x)$ is monotonic over a wide range of depths. Physically, the spectrum is broad because of the random nature of the stopping mechanism for electrons in solids—electrons may arrive at the surface with equal energies yet originate from different depths. Nevertheless, selective depth profiling can be made much more effective by subjecting the experimental results to mathematical analysis; in particular, thin internal layers can be localized and selected for study.

We will illustrate the method in two cases, in which only surface layers and deep layers are to be analyzed, respectively (in the latter case, there should be no surface contribution to the signal). This can be accomplished if we have two groups of electrons with the yield functions $P(x)$ shown in Fig. 6—for one group, $P(x)$ is localized near the surface (a), while for the other, $P(x)$ is nearly zero for small x (b).

Although these two groups are fictitious, their $P(x)$'s can be constructed as superpositions of the $P(x)$ for the actual electrons. In other words, they can be expressed as linear combinations of the experimentally recorded $P(x)$ (Fig. 3) with coefficients determinable by the same technique

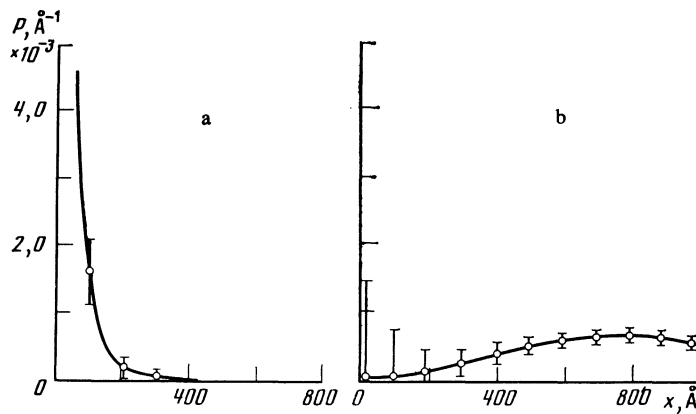


FIG. 6. The localized surface and volume depth profiles $P(x)$, obtained by superposing the experimental profiles P_i . a) thin surface layer of width $\Delta d < 100 \text{ \AA}$; b) interior layer at depth $d > 300 \text{ \AA}$. The bars indicate the error in $P(x)$ due to errors in measuring $P_i(x)$.

used to calculate Fourier coefficients. We calculated the coefficients on a BÉSM-6 computer and found that the "surface" and "volume" yields P_s , P_v corresponding to Fig. 6a and Fig. 6b can be expressed as

$$P_s(x) = -16.2 P_1(x) + 12.7 P_2(x) + 4.5 P_3(x), \quad (5a)$$

$$P_v(x) = -137.8 P_1(x) + 50.6 P_2(x) + 88.2 P_3(x). \quad (5b)$$

in terms of the experimental P 's.

These superpositions are useful, because if we replace the experimental values $P_i(x)$ by arbitrary experimental data (Mössbauer spectra of conversion electrons, $\chi(\theta)$, etc.) obtained for electrons with final energies E_f in the same ranges i , the left-hand sides of (5a) and (5b) will give the resultant surface and volume signals, respectively. The contribution from the signals for the other electrons is eliminated and does not appear in the final result.

Figure 7 shows some angular dependences $\chi(\theta)$ found by the above method. Curve 1 is a superposition of the experimentally measured $\chi(\theta)$ (Fig. 3, curves 1–3), weighted with the coefficients in (5a). The behavior is as expected— χ increases rapidly as $1/\sin \theta$ for small yield depths. On the other hand, the superposition (Fig. 7, curve 2) with the weight coefficients in (5b) corresponds to electrons that originate from the interior of the target. This can be seen from the very long plateau, which as shown above should be present for yield depths x greater than the field penetration distance.

The superposition technique can thus enhance the use-

fulness of depth profiling considerably even if only a few functions are superposed. It is important to note that the layer localization error in the superposition method depends on how accurately the experimental $P_i(x)$ are measured. The rather large errors (17 and 7%) in our experiment were due to the fact that the total number of measurements was too small. This is reflected in the large error bars for the surface and volume superpositions in Fig. 6. More accurate measurements will make it possible to substantially decrease the error in specifying the required depth profiles. By experimentally measuring the yield functions for a larger number of energy ranges (so that more terms can be used in the superpositions), the layers can be localized more precisely and the capabilities of the technique enhanced, so that one can record not only the surface signal but also signals from arbitrary, well-localized deep layers. Figure 8 shows the results from model calculations of localization for internal layers. The model assumes five groups of electrons with different maximum yield depths. The depth x (equal to 3 arbitrary units) was greatest for the first group (Fig. 8a). This low-energy group was treated in the model as an ensemble of electrons and was integrated over E_f ; the other four groups 2–5 corresponded to electrons with successively decreasing energy losses, $x = 2.4, 1.8, 1.2, \text{ and } 0.6$, respectively. Using these yield functions, we were able to select the signal from a layer of width 0.5 at depth 0.5, i.e., from a layer of width 6 times less than the maximum depth for the entire electron population. The depth profile of this layer is shown in Fig. 8b, which also indicates the possible errors in $P(x)$ for initial yield functions measured to various accuracy.

7. CONCLUSIONS

The pronounced differences among the measured angular dependences $\chi(\theta)$ of the photoemission near the critical angle (Fig. 3, curves 1–3) indicate that $\chi(\theta)$ is sensitive to the yield depth x of the electrons. This sensitivity can be exploited to accurately determine the yield functions. In addition to being highly accurate, our method for measuring $P(x)$ is also simple and generally applicable. The measurements can be carried out on nearly any material with a sufficiently smooth surface, and they are simple because all the needed data can be obtained in a single experiment without changing samples.

The results can be used directly in Mössbauer experi-

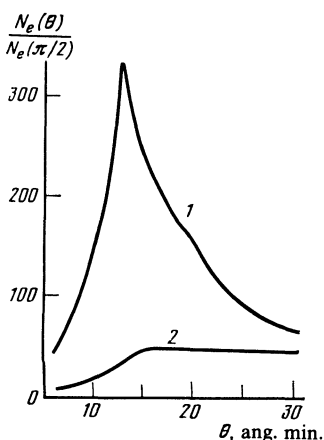


FIG. 7. Normalized photoemission $\chi(\theta)$ found by superposing the experimental profiles. Curves 1 and 2 give $\chi(\theta)$ for the localized layers with the depth profiles shown in Fig. 6a and 6b, respectively.

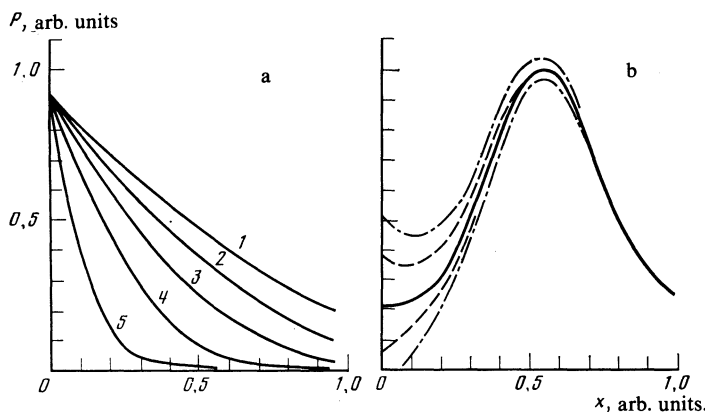


FIG. 8. Results from model calculations illustrating the improved localization achieved by superposition. a) The five model functions $P_i(x)$, which correspond to wide, unlocalized layers. b) Signal from a narrowly localized layer (solid curve in Fig. b) obtained by superposing the five model functions. The dashed and dashed-dotted curves show the errors in specifying the layer profile, assuming 1% and 3% errors, respectively, in measuring the initial yield probabilities $P(x)$.

ments. The primary error in simulating the conditions in Mössbauer experiments is negligible and arises because the energy of the monochromatic beam selected from the white x-ray bremsstrahlung may not coincide exactly with the energy of the nuclear transition. This error is thus determined by the error in setting the required Bragg angle and can be decreased to 10^{-3} or less.

The improved layer localization achieved by superposing the experimental results offers a new approach to the design of experiments in which Mössbauer conversion-electron spectroscopy is used for selective depth profiling. Previously, the principal method for improving the localization was to increase the energy resolution of the electron detectors. However, in this case only signals from the layers closest to the surface could be selected, because electrons reaching the surface with identical final energies may nonetheless have very different pathlengths through the material. Indeed, the spread $\Delta\lambda$ is comparable to the mean free path $\bar{\lambda}$.¹⁵ Well-localized layers could therefore be analyzed only to shallow depths 0–200 Å. Another factor which has held back depth profiling for large x is the fact that the energy spectrum corresponds to different groups of electrons at lower energies; although these electrons have the same E_f , their characteristic pathlengths λ differ. Selective analysis therefore required using a range of energies containing only one such group (e.g., the range 6.3–7.3 keV for ^{57}Fe). The characteristic yield depth of these electrons is also several times less than the maximum value of λ .

In addition to limiting the range of depths that can be analyzed, layer localization based on improved energy resolution has the disadvantage of substantially decreasing the solid angle of the receiver, so that the measurement time is greatly increased.

By contrast, the superposition method enables one to employ comparatively simple and inexpensive detectors (such as proportional gas counters) with moderate energy resolutions. Because of their wider apertures, the measurement time is greatly decreased and enough data can be accumulated in a reasonable time to ensure that the starting yield functions used in the superposition method are accurate. The fundamental feature of the superposition method is that

signals can be selected from thin layers both near the surface and at arbitrary depths.

The superposition and energy-resolution methods for layer localization in selective depth profiling represent two extreme approaches to experimental design. Precise information from sharply localized layers should be obtainable in less time by using the two methods to complement each other in optimized experiments, in which the energy resolution and relative aperture of the electron detector are chosen to achieve specific counting rates, signal/noise ratios, etc.

¹⁾The radiation field may penetrate to this depth under these conditions.

²⁾ $I_0(\theta)$ is exactly equal to 1 for θ above the critical angle, for which there is no reflected wave.

³⁾M. J. Tricker, in: Symp. on Mössbauer Spectroscopy and Chemical Applications (J. G. Stevens and G. K. Shenoy, eds.), Am. Chem. Soc. (1981), p. 63.

⁴⁾H. G. Wagner, M. Ackermann, and U. Gonser, Non-Cryst. Sol. **61-62**, 847 (1984).

⁵⁾G. V. Smirnov and A. I. Chumakov, Zh. Eksp. Teor. Fiz. **89**, 1169 (1985) [Sov. Phys. JETP **62**, No. 4 (1985)].

⁶⁾T. Yang, A. Krishnan, N. Benczer-Koller, and G. Bayreuther, Phys. Rev. Lett. **48**, 1292 (1982).

⁷⁾E. Kh. Mukhamedzhanov, A. V. Maslov, A. N. Chuzo, and R. M. Imamov, Poverkhnost' **3**, 54 (1984).

⁸⁾A. I. Chumakov, G. V. Smirnov, M. V. Kruglov, and I. K. Solomin, Fiz. Tverd. Tela (Leningrad) **26**, 746 (1984) [Sov. Phys. Solid State **26**, 451 (1984)].

⁹⁾A. M. Afanasev, R. M. Imamov, and E. Kh. Mukhamedzhanov, Phys. Status Solidi (a) **83**, K5 (1984).

¹⁰⁾Y. Yonekura, T. Toriyama, J. Itoh, and K. Hisatake, Hyperfine Interaction **15/16**, 1005 (1983).

¹¹⁾I. K. Solomin and M. V. Kruglov, Fiz. Tverd. Tela (Leningrad) **26**, 519 (1984) [Sov. Phys. Solid State **26**, 310 (1984)].

¹²⁾I. K. Solomin, M. V. Kruglov, A. I. Chumakov, and G. V. Smirnov, in: Proc. 19th All-Union Conf. on Emission Electronics, Tashkent (1984), p. 84.

¹³⁾D. Liljequist, "Electron penetration in solids and its application to Mössbauer spectroscopy," USIP Report, Stockholm (1979), p. 34.

¹⁴⁾N. I. Kaliteevskii, Volnovaya Optika (Wave Optics), Nauka, Moscow (1971), p. 78.

¹⁵⁾A. I. Chumakov, A. B. Dubrovin, and G. V. Smirnov, Nucl. Instr. Meth. **216**, 505 (1983).

¹⁶⁾J. P. Hannon, G. T. Trammel, M. Mueller, et al., Phys. Rev. Lett. **43**, 636 (1979).

¹⁷⁾D. Liljequist and M. Ismail, Phys. Rev. B **31**, 4131 (1985).

Translated by A. Mason